Photoinduced two-photon absorption and second-harmonic generation in As_2Te_3-$CaCl_2$-$PbCl_2$ glasses

I. V. Kityk
Institute of Physics, University WSP, Aleja Armii Krajowej 13/15, PL-42201 Częstochowa, Poland

B. Sahraoui
University of Angers, Laboratory POMA, CNRS EP 130, UFR Sciences, 2, Boulevard Lavoisier, 49045 Angers, Cedex 01, France

(Received 22 December 1998)

Photoinduced nonlinear optical phenomena in amorphous As_2Te_3-$CaCl_2$-$PbCl_2$ glasses have been studied using experimental and theoretical quantum chemical and molecular-dynamics methods. Especially photoinduced two-photon absorption (TPA) and second-harmonic generation (SHG) were measured in the IR region from 5.5–21 μm. CO laser ($\lambda=5.5\,\mu$m) and parametrically generated wavelengths (5.2–13.7 μm) were used as a source of pumping light. We have found that with an increase of photoinducing power, the SHG for probe CO_2 laser (for the double frequency $\lambda=5.3\,\mu$m) signal increases and achieves its maximum value at photoinducing power 1.45 GW/cm^2 per pulse. The absolute values of the SHG were more than one order less comparing to χ_{222} tensor for Ag_3AsSe_3 single crystals. With decreasing temperature, the SHG signal strongly increases within the 16–24 K temperature range. Femtosecond probe-pump measurements indicate on an existence of SHG maximum at pump-probe time delay about 25 ps. Spectral positions of the TPA maxima are strongly dependent on the pump power. Contrary to the SHG behavior, for the TPA we observe at least two time delayed maxima: at 20–27 and 65 ps. We explain these dependencies within a framework of the quantum chemical approach taken into account with photoinduced anharmonic electron-vibration interaction. We have revealed that As-Te tetrahedra play a key role in the observed photoinduced nonlinear optics effects. The obtained results show that the mentioned effects can be used as a powerful tool for investigations of picosecond IR nonlinear optics processes. Simultaneously the investigated glasses are promising materials for IR femtosecond quantum electronics. [S0163-1829(99)05325-4]

I. INTRODUCTION

As_2Te_3-$CaCl_2$-$PbCl_2$ glasses[1–3] promise to be perspective materials for IR optoelectronics and quantum electronics due to the possibility of their use in different branches of IR optoelectronics, holography, and IR quantum electronics materials engineering, particularly as a material for IR fibers. The range of light transmission T of the obtained glasses falls within the range 0.65–40 μm at the level 25–50 % (see Fig. 1). They possess high photomechanical stability (up to 4.1 GW/cm^2).[2]

These glasses, due to peculiarities of their chemical content,[4,5] could be interesting for IR photoinduced effects. Some physical and chemical properties of the mentioned compounds were described by several authors,[1,2] but to our knowledge, there is no work devoted to the influence of external IR laser light on their basic optical properties, particularly on nonlinear optical susceptibilities. The problem of photoinduced changes in glasses is well developed for chalcogenide glasses and As_2Se_3 particularly.[6–14] But in the mid-IR spectral range the nature of photoinduced changes of the optical properties of glasses remains unknown. As a consequence in the present work we perform the photoinduced nonlinear optics measurements in the As_2Te_3-$CaCl_2$-$PbCl_2$ glasses to test a possibility to use this material for IR nonlinear optics electronics. To clarify mechanisms and origin of the photoinduced effects and contribution of particular structural clusters as well of vibration and electronic subsystems we perform *ab initio* electron structure calculations with simultaneous molecular-dynamics geometry optimizations. Especially we should clarify the role played by IR harmonic and electron-harmonic interactions on the observed phenomena, particularly during the high-resolved femtosecond temporary effects.

We perform complex investigations of IR photoinduced influence on nonlinear optical properties; particularly we investigate the optical second-harmonic generation (SHG), described by the polar third rank tensors, and two-photon absorption (TPA), described by imaginary part of fourth-rank nonlinear optical tensors, in order to clarify the physical mechanisms responsible for the photoinduced changes in the middle infrared spectral range.

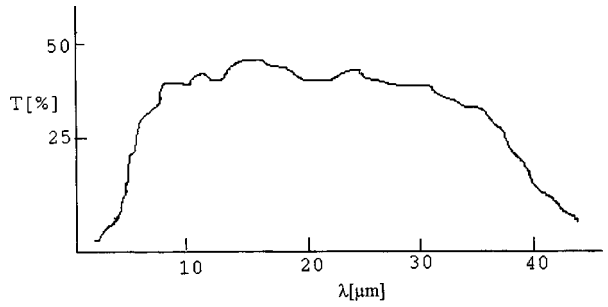

FIG. 1. Phototransparency T of the As-Te-$CaCl_2$-$PbCl_2$ glasses.

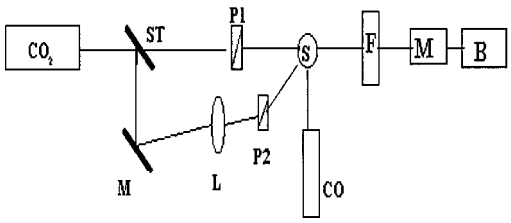

FIG. 2. Experimental setup used for the measurements of the photoinduced SHG and TPA in the investigated glasses.

In Sec. II we briefly describe specimen preparation and experimental nonlinear optical methods. The experimentally obtained results for the photoinduced SHG, TPA versus pump intensity, temperature, and delaying time are presented in Sec. III. Theoretical analysis of physical mechanisms causing the photoinduced nonlinear optics effects on a ground of *ab initio* quantum chemical calculations and molecular-dynamics simulations is presented in Sec. IV.

II. EXPERIMENTAL DETAILS

A. Sample preparation

The investigated glasses are synthesized by methods described in Ref. 1. The upper and lower limits of As_2Te_3 concentration for bulk glass formation is 12.0 and 25 mol %, respectively. The third compound $CaCl_2$ enhances the glass forming tendency of the binary system. The binary system As_2Te_3-$CaCl_2$ cannot form bulk glass due to the higher field strength of the Ca^{2+} ion. Concentration of $PbCl_2$ was varied within 12–21%. Specimen homogeneity determined by x-ray diffraction (XRD) and optical polarized methods is about 6.5%. Maximal average sizes of the samples vary within the sizes $5\times3\times7$ mm^3. Scattering background was less than 0.4%.

B. Experimental technique

The experimental equipment for performing photoinduced measurements of nonlinear optical susceptibilities is shown in Fig. 2. We use two different kinds of pump and probe light. In the first type, light from CO_2 laser is split by a semitransparent ZnSe plate (ST) into two beams: the first one is propagated through the polarizer $P1$, the second one is doubled or parametrically passed through the linear (L) wavelength parametrical Ag_3AsSe_3 generator, that gives light with continuous wavelength varying within the spectral range 7–15 μm. This beam propagates through the sample S and interacts with the glass sample. Therefore we are able to detect an interaction between the pump and probe laser beams and to detect the wavelength mixing two-photon processes, that give information concerning the nature of the observed TPA processes. In the second experimental geometry, we use a pulsed CO laser ($\lambda=5.5\,\mu$m, $P=12-29$ MW, $\tau=0.44-80$ ps, frequency repetition 8–15 Hz) with wavelength of 5.5 μm for IR pumping light. The probe CO_2 laser beam ($\lambda=10.6\,\mu$m, $P=46$ MW, $\tau=0.9-50$ ps, frequency repetition 8–15 Hz) is used to calibrate the observed nonlinear optical output signal. The laser frequency and pulse duration is chosen to avoid a local nonequilibrium specimen overheating. Control of the pulse energy is performed using a boxcar IR bolometer with the gain time of 374 ps. The presented data are obtained after averaging over the large sample surfaces (up to 1.0 cm^2). The absolute value of the output photoinduced SHG is about 10^{-8} compared with the input probe CO_2 intensity. The optimal sample thickness for achievement of maximal SHG signal lies within the 1.24–2.76 mm range.

Using a ZnSe beamsplitter and proustite delaying line, the CO_2 laser beam was split into two beams at 10.6 μm. Our apparatus (see Fig. 2) allows us to vary delay time between the pump and probe light for the different wavelengths. At the same time, the equipment allows us continuously to vary light power and light polarizations. The IR energy fluence is controlled using the GENETIC 5.M electronic boxcar with gate about 220 ps.

The separation between the output SHG ($\lambda=5.3\,\mu$m), pumping CO ($\lambda=5.5\,\mu$m) or (5–13 μm) light is achieved using an IR grating monochromator IRG-8.96-M with spectral resolution of 0.055 μm/mm. The SHG intensity is measured independently using digital RIR-34 IR bolometer with accuracy up to 220 quanta per pulse.

The TPA signal is obtained from the pump-dependent absorption features. The measurements are carried out in the single-pulse regime, with a pulse frequency repetition of 8 Hz and the tunable pulse duration within 3.7–79 ps. To evaluate TPA coefficient β we use the expression $PT\approx1-\beta\ell I_p$, where ℓ is the thickness of investigated sample, and PT is intensity dependent phototransparency for pumping wavelength.

For each pulse we measure separately the signals of the pump, probe, and output pump plus probe intensities. After over-the-surface averaging we obtain the values of the TPA coefficient. We extract scattered and reflected background assuming Gaussian-like shape of the probe CO_2 laser beam. Stability of laser intensity is higher than 0.6%. But in order to avoid errors connected with the specimen nonhomogenates we will present the obtained nonlinear susceptibilities (SHG and TPA) in the arbitrary units. We vary also laser spots within the 80–200 μm to exclude different diffraction phenomena. All the specimens are supplied by additional thermopower bolometer for control of specimen heating. As a criterion of thermostability we have chosen relative local temperature changes less than 0.1 K.

We carry out the measurements for fixed pumping wavelength of 10.6 μm and by varying the probe wavelength within the spectral range 5–20 μm. Degree of polarization for the pumping and probing light is equal to 96–98 % depending on the spectra wavelength.

As a consequence, we are able to vary light polarizations both for incident as well as for output light. The pumping and probing beams are synchronized in time within 450 fs. The bolometer integrates the energy fluence with a time resolution up to 0.45 ps. Intensities of the beams were changed using the proustite prisms. Time delay between the pump and probe beam is changed by ZnSe delaying line. All the detection is carried out using high-time-resolved spectroanalyzer SA-165 connected with the 40 ps gained boxcar.

III. EXPERIMENTAL RESULTS

The measured dependencies of the photoinduced SHG intensities ($\lambda=5.3\,\mu$m) as a function of pump pulse CO laser

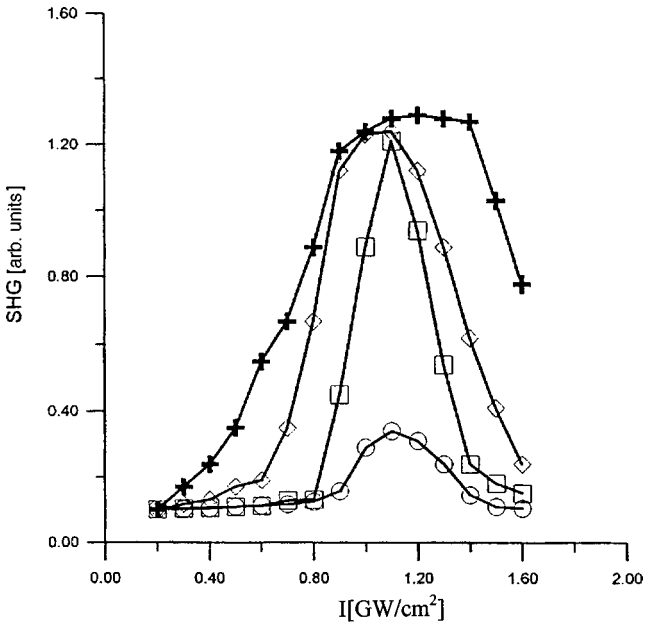

FIG. 3. Dependences of the photoinduced SHG at $\lambda = 5.3\ \mu$m, in arbitrary units, versus photoinducing CO laser and temperature: (+) 4.2 K; (◇) 8.6 K; (□) 16.3 K; (○) 22.4 K. All the measurements correspond to the time delay between the probe and the pump light of about 25 ps.

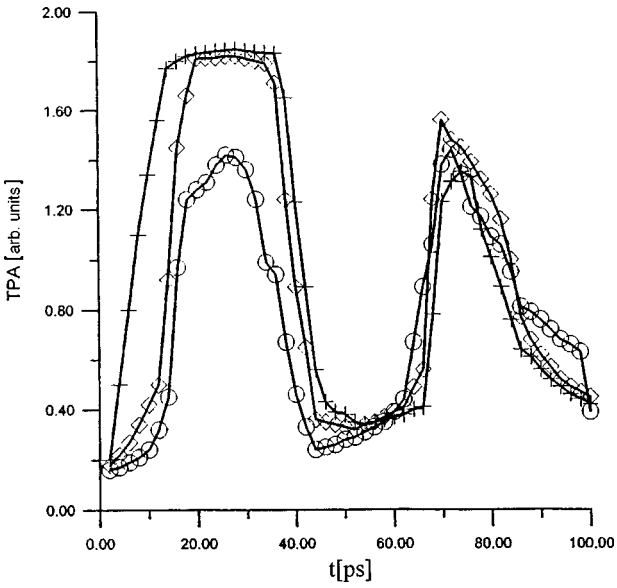

FIG. 4. Dependences of the photoinduced TPA at $\lambda = 5.3\ \mu$m, in arbitrary units, versus pump-probe time delay at different temperatures: (+) 4.2 K; (◇) 8.6 K; (○) 16.3 K.

($\lambda = 5.5\ \mu$m) integrated exposure time for different pump fluences are presented in Fig. 3. We have found that with increasing power of the pump CO-laser pulses the SHG maximum output signal increases and achieves its maximum at CO photon fluxes within the 0.86–1.38 GW/cm^2 densities per pulse. Maximal output SHG signal is observed for collinear polarizations of probe and pump light beams and incident angles lying within 3–6°. We have revealed also that the lowest scattered background was obtained for the spot of probe laser beam about 92–94 μm. All the photoinduced changes are reversible with precision up to 0.014% (controlled by the phototransparency).

The maximal intensity of the output SHG is achieved for the time delays about the 27 ps and at low temperatures (below 20 K). The results are presented versus temperature and one can clearly see that decrease of temperature below 22 K enhances the output SHG signal at least four times. At 16.3 K the shape of the SHG is very sharp versus the pump light intensity. The next decrease of the temperature below 10 K leads to appearance of a flat maximum within the 1.18–1.53 GW/cm^2 at $T = 4.2$ K. At temperatures higher than 60 K the SHG signal is commensurable with the light-scattering background. One can see also several asymmetries in the observed behaviors. The maximal observed absolute SHG values are more than one order less compared with $Ag_3As_SSe_3$ crystals for the χ_{222} ($\lambda = 10.6\ \mu$m) nonlinear optical susceptibility tensor components. The photoinduced SHG signal relaxation time does not exceed 0.9 ps and decreases up to 0.6 ps for temperatures higher than 35 K. All the measurements are done during CO pump illumination and the presented values correspond to maxima of the SHG output signal after statistical averaging through the specimen surfaces. For each point we obtain the statistics of more than 120 points. The χ^2 parameter of student statistics was not worse than 5%.

To investigate fourth-order nonlinear optical effects we measure TPA for geometry corresponding to the χ_{xxxx} tensor component corresponding to collinear polarizations of the pump and probe beams. The off-diagonal χ_{xxyy} tensor components show the output signal at least half an order weaker.

Continuously varying time delay between the pump and probe beams we observe two TPA maxima (see Fig. 4). The first one occurs at a delay time range within 18–41 ps and continuously increases up to 10–48 ps with decreasing temperature up to liquid helium temperature (LHeT). Several similarities between the temperature dependences for the photoinduced SHG and the mentioned TPA maximum could be observed. The second time-dependent TPA maximum is temperature (4.2–17 K) independent (within the 62–99 ps). This narrow maximum shows a weak temporary asymmetry. For delaying times higher than 100 ps the output TPA signal becomes very low (comparable with the noise background). The absolute TPA values are changed within 1.27–1.44 cm/GW.

To understand the spectral distribution of the TPA signal we carry out measurements versus the wavelength (within the spectral range 10–40 μm) at different temperatures (see Fig. 5). All the measurements were conducted for the delaying time at about 22 ps. One can see that the maximal TPA signal is achieved within the spectral range 21–24.5 μm at $T = 4.2$ K and its range increases up to 18–33 μm for LHeT. This fact indicates on a correlation between the temperature and the IR modes. For reliability we control the signal at 10.6 μm as well as 5.3 μm.

Picosecond relaxation times indicate substantial contribution of electronic subsystem playing in the observed photoinduced changes. As a consequence the photoexcited vibrations contribute to the time-resolved susceptibilities due to a high value of electron-vibration interaction constants and high concentration of photoinduced vibration modes. Stability of the observed spectral dependences was higher than 0.2 μm. Intensities of the photoinduced IR modes are repro-

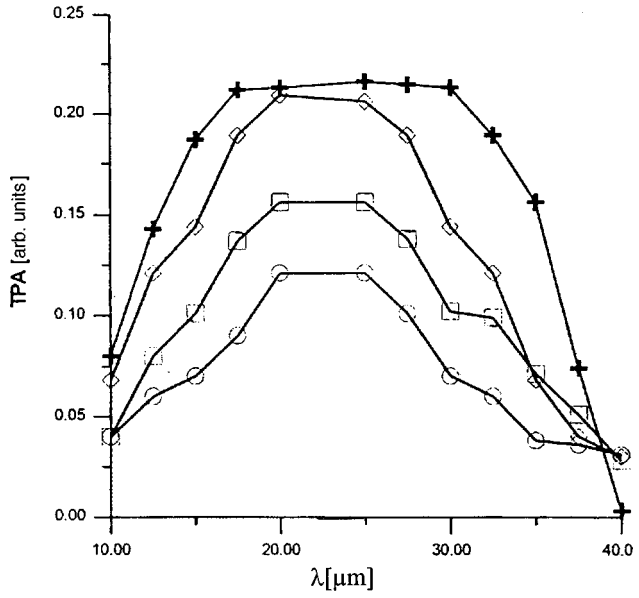

FIG. 5. Spectral dependences of the TPA, in arbitrary units, at different temperatures: (+) 4.2 K; (◇) 8.6 K; (□) 16.3 K; (○) 22.4 K.

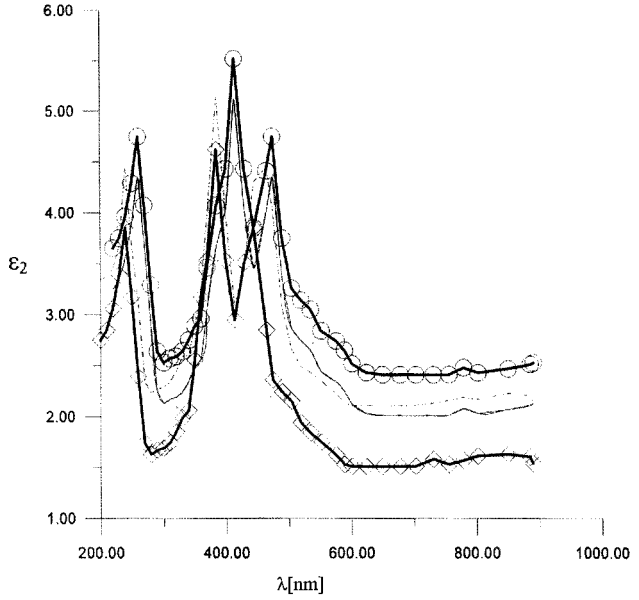

FIG. 6. Spectral dependences of imaginary part of dielectric susceptibility $\varepsilon_2(E)$: (○) before IR photoexposure; (◇) during IR photoexposure of 1.2 GW/cm^2; (—.—.—.—) theoretically calculated without inclusion of excited states; (— — —) with taken into account the configuration interactions.

duced with reliability of about 3.6%. All the measurements are made during illumination. They show the full reversibility after the applied photoinducing signal. In multiple photoexposure-thermoannealing cycles these changes of optical density can be repeated with a small irreversible component (of 0.1–0.24 %).

IV. THEORETICAL SIMULATION AND DISCUSSION

The above-obtained experimental data unambiguously show essential influence of vibration subsystem on the nonlinear optical susceptibilities. At the same time electron vibration should play an essential role (quasiphonon interactions). Therefore in our considerations we will pay special attention to electron-quasiphonon interactions, particularly to anharmonic renormalizations of vibration subsystems.

We carry out molecular-dynamics geometry optimizations using the hybrid Becke's method[17–22] involving the starting basis from the GAUSSIAN 94 program.[23] Polarized correlation consistent double ς basis[24] is used within the discrete Fourier transform (DFT) procedure. Geometrical parameters obtained by the mentioned method are proven to reproduce the experimental RDF data (see Table I) within 0.07 Å. The nondynamic correlations are taken into account within the multiconfiguration self-consistent-field (MCSCF) approach included in the GAMES program.[25] On the ground of the optimized structural geometry appropriate eigenenergies and eigenvectors are calculated. The latter are used for evaluation of the electron-vibration states playing a chief role in the nonlinear optical susceptibilities. The long-range contributions are taken into account using the quasicrystalline approach successfully applied by us to the different disordered media.[3,15,25–27]

TABLE I. Experimental RDF distances for the first and second coordination sphere of the main chemical bonds.

Chemical bond	First coordination sphere |Å|	Second coordination sphere |Å|
As-Te	2.563(5)	3.248(6)
Pb-Cl	2.514(8)	3.302(3)
Ca-Cl	2.814(2)	3.567(6)
Te-Te	3.001(3)	4.086(1)
Pb-Pb	3.008(2)	4.124(9)
Cl-Cl	2.899(7)	4.568(0)

As a criterion of the quality of our model we compare the calculated by the mentioned method spectra of the imaginary part of dielectric optical susceptibility $\varepsilon_2(E)$ with the experimental spectra obtained from ellipsometry measurements (see Fig. 6). In Fig. 7 are presented corresponding dependencies of $\varepsilon_2(E)$ obtained experimentally and calculated with inclusion of the long-range solid-state interactions. One can see a good agreement between the theory and experiment. Several discrepancies in absolute values and shapes reflect probably electron-quasiphonon renormalization. With increasing IR photoinducing power one can see several shifts of the main optical modes originated prevailingly from the $4s$As-$5p$Te electronic terms. This confirms the essential role of strong electron-quasivibration interaction in the observed phenomena. In the calculated spectra we are not able to take into account trapping levels of essentially modified obtained spectra.

Therefore we perform calculations for the vibration basis set remormalized by electron subsystems. Second derivatives of an electrostatic cluster potential with respect to given normal coordinates are calculated numerically with precision up to 0.0021 hartree for the main chemical bonds presented in Table I. The latter are used for determination of force constants. An eigenenergy of the kth vibration mode is expressed as

$$\Omega_k(\nu_k)=2\Omega_{k0}(\nu_k+\tfrac{1}{2}), \tag{1}$$

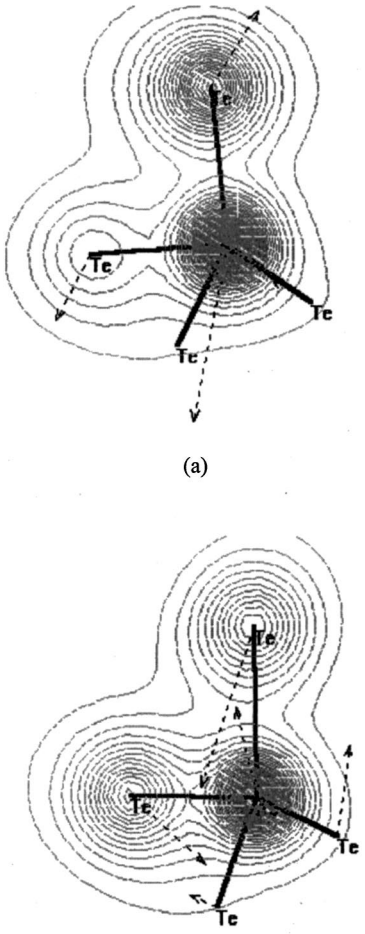

FIG. 7. Changes of electronic charge-density distribution for the $AsTe_4$ clusters: (a) before photoexposure and (b) after photoexposure with an increment $0.45\,e/\Omega$.

where $\Omega_{k0}=(h/2\pi)(f_k/\mu_k)^{-1/2}/2$ is the zero-point motion energy and $\nu_k=0,1,2,\ldots$ is the vibration quantum number associated with the following wave function:

$$\Psi_k(Q_k)=(2\Omega_{k0}/\pi)^{1/4}(2^{\nu_k}/\nu_k!)^{-1/2}\times\exp(-\Omega_{k0}\Omega_k^2)H_\nu[(2\Omega_{k0})^{1/2}Q_k], \quad (2)$$

where $H_\nu(x)$ is the Hermite polynomial. The obtained harmonic vibration wave functions serve as a basis for the following evaluations of electron-vibration interactions.

An electron-phonon interaction potential was calculated in a nonlinear approximation:

$$V_{e\text{-}ph}(\mathbf{r}_i)=e^2\sum_{ms} M_{ms}^{-1/2}\left[Z_{ms}(\mathbf{r}_s-\mathbf{u}_{ms})|\mathbf{r}_s-\mathbf{u}_{ms}|^{-3} - \sum_{m's'} Z_{m's'}(\mathbf{r}_{s'}-\mathbf{u}_{m's'})|\mathbf{r}_{s'}-\mathbf{u}_{m's'}|^{-3}\right], \quad (3)$$

where M_{ms} and Z_{ms} are the effective ionic mass and charge; the corresponding ions are numbered by m and s, respectively. The $\mathbf{u}_{ms,m's'}$ vector is a relative displacement of two ions from their equilibrium positions $\mathbf{r}_s$ and $\mathbf{r}_{s'}$. Probability of a one-phonon transition is equal to

$$W^-(\Omega_k)=4(h/2\pi)^{-2}c^{-3}H^{-1}g^{-1}(\mathbf{r}_i)(E_{\mathrm{IR}}-\Omega_k)^2B^-(\Omega_k), \quad (4)$$

where H is a sum of the η and ξ levels widths, E_{IR} is an energy of the IR photoinducing beam, Ω_k denotes a kth vibration energy and $g(r_i)$ is a degeneration degree of the corresponding electron energy levels.

The parameter $B^-(\Omega_k)$ is equal to

$$B^-(\Omega_k)=\sum_{\eta}^{g(\eta)}\sum_{\xi}^{g(\xi)}\left|\left\{\sum_{\varphi}\langle\eta,\eta_\Omega|V_{e\text{-}ph}(\mathbf{r}_i)|\varphi,\eta_{\Omega+1}\rangle\langle\varphi|\mathbf{d}|\xi\rangle \times(E_\xi-E_\eta+\Omega_k)^{-1}+\sum_{\varphi}\langle\eta|\mathbf{d}|\varphi\rangle \times\langle\varphi,\eta_\Omega|V_{e\text{-}ph}(\mathbf{r}_i)|\xi,\eta_{\Omega-1}\rangle \times(E_\xi-E_\eta-\Omega_k)^{-1}\right\}\right|^2\theta, \quad (5)$$

where φ denotes a virtual intermediate excited vibration state, $\mathbf{d}$ is an electric dipole moment for a given optical transition; η_Ω and η,φ,ξ correspond to electronic and vibration states, respectively. The sums are performed over all degenerated initial and final states. The notation θ denotes an average with respect to occupation numbers of the quasiphonon states for quasiphonons with frequency Ω_k. In order to take into account occupation dynamics due to photoinduced changes we build the systems of population differential equations:

$$dn_0/dt=-\sum_\alpha A_{0\alpha}\int[B_{0\alpha}(t-\tau)In_\alpha]+\sum_\alpha(A_{0\alpha}n_\alpha), \quad (6)$$

$$dn_\alpha/dt=-\sum_\beta A_{\beta\alpha}\int[B_{\alpha\beta}(t-\tau)In_\beta]+\sum_\beta(A_{\alpha\beta}n_\alpha), \quad (6a)$$

where I is the power density of IR photoinducing power, the occupation of the ground states n_α is the population of the αth state, and τ is delaying time between the pump and probe beams. Coefficients of the $B_{0\alpha}$ and $A_{0\alpha}$ are induced and spontaneous Einstein coefficients between the ground (0) and excited (α) states are

$$A_{0\alpha}=8\pi\omega^3|\mathbf{d}_{0\alpha}|^2n_{eo}n_{pho}(1-n_{e\alpha})(1-n_{ph\alpha})/3hc^3,$$

$$B_{0\alpha}=c^3A_{0\alpha}/\pi h\omega^3. \quad (7)$$

Here n_{co} and n_{pho} correspond to the Fermi-Dirac and Bose-Einstein carrier distribution of the ground state for electronic and vibration states, respectively. These terms include the temperature-dependent term. We have taken into account 24 relatively stronger IR oscillators. As a consequence we resolve the set of 24 differential equations taking into account the broader conditions.

Our calculations show that the dominant role in the corresponding photoinduced optical susceptibilities give the As-Te cluster because only for the mentioned cluster is essential redistribution of the electronic charge density under photoillumination observed (see Fig. 7). For the Ca-Cl and Pb-Cl clusters the changes are relatively small (smaller than

2.4%). This is confirmed by calculation of the matrix dipole moment that in the case of the As-Te cluster is equal to 0.975 D. At the same time, for the Ca-Cl and Pb-Cl clusters the total dipole momentum is equal 0.03 and 0.08 D, respectively.

Therefore we can conclude that the As-Te clusters play a dominant role in the appearance of the observed photoinduced changes for the investigated glasses. Moreover, from comparison of Fig. 7(a) with Fig. 7(b) one can observe an appearance of local noncentrosymmetry (acentricity) in the electronic charge-density distribution. The latter is very important for the nonlinear optical susceptibilities.

To understand the temperature dependencies we consider the contributions of the vibrations subsystems both due to the harmonic as well due to the anharmonic electron-vibration contributions:

$$B^{-}(\Omega_k)=C^{\gamma}_{\eta\xi}(r^{\Delta}_{\lambda})C^{\gamma'}_{\eta\xi}(r^{\Delta'}_{\lambda'})\,\mathrm{Im}\,G^{\gamma\gamma'}_{\Delta\Delta'}(r^{\Delta}_{\lambda},\Omega^2_k), \tag{8}$$

where $G^{\gamma\gamma'}_{\Delta\Delta'}(r^{\Delta}_{\lambda})$ is a Green function (γ and γ' are numbers of coordination sphere) defined as

$$G^{\gamma\gamma'}_{\Delta\Delta'}(r^{\Delta}_{\lambda})=\sum_{\varphi}\{\langle\eta|V_{e\text{-}ph}(\mathbf{r}_i)|\varphi\rangle\langle\varphi|\mathbf{d}|\xi\rangle + \langle\eta|\mathbf{d}|\varphi\rangle\langle\varphi|V_{e\text{-}ph}(\mathbf{r}_i)|\xi\rangle\}(E_{\xi}-E_{\eta})^{-1}. \tag{9}$$

The resulting expression is

$$G^{\gamma\gamma'}_{\Delta\Delta'}(r^{\Delta}_{\lambda},\Omega^2_k)=\sum_{\Omega}K^{\gamma'}_{\Delta'}(r^{\Delta}_{\lambda})K^{\gamma}_{\Delta}(r^{\Delta}_{\lambda})(\Omega^2_k-\Omega^2-i\delta)^{-1}, \tag{10}$$

where the coordinates $K^{\gamma}_{\Delta}(r^{\Delta}_{\lambda})$ are obtained for a given vibration type from the states renormalization. Numerical calculations are performed with accuracy up to 0.02 hartree.

To include the lattice deformations into the Green function, we take into account deformation localization allowing us to use the Dyson relations.[28] The deformation potential and corresponding charge defect perturbance determine the potential operator U and

$$G^{\gamma\gamma'}_{\Delta\Delta'}(1)=G^{\gamma\gamma'}_{\Delta\Delta'}(0)+G^{\gamma\gamma'}_{\Delta\Delta'}(0)UG^{\gamma\gamma'}_{\Delta\Delta'}(1), \tag{11}$$

where $G^{\gamma\gamma'}_{\Delta\Delta'}(0)$ and $G^{\gamma\gamma'}_{\Delta\Delta'}(1)$ are the Green functions for harmonic subsystems and disturbed by anharmonic electron-vibration potential U, respectively.

The relation between the real and imaginary parts of the Green function are obtained using Kramers-Kronig dispersion relations. In order to explain the observed dependencies it is necessary to carry out evaluations of the time-dependent nonlinear optical susceptibilities. Calculations of the third and fourth rank nonlinear optical susceptibility tensors have been carried out using the following expressions:[16]

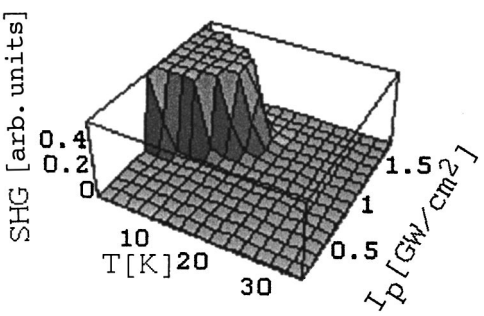

FIG. 8. Theoretically calculated dependences of the photoinduced SHG for $\lambda=5.3\,\mu$m, in arbitrary units, versus the intensity of the photoinducing CO laser I_p and temperature T.

$$\chi^{(\omega,\omega)}_{ijk}=\frac{1}{\hbar^2}\frac{e^3N}{2!}\hat{P}_{ijk}\sum_{k}\sum_{\alpha,\beta}\left(\frac{\langle 0|i|\alpha\rangle\langle\alpha|j|\beta\rangle\langle\beta|k|0\rangle}{(2\omega+\omega_{\alpha})(\omega+\omega_{\beta})} + \frac{\langle 0|j|\alpha\rangle\langle\alpha|i|\beta\rangle\langle\beta|k|0\rangle}{(\omega_{\alpha}-2\omega)(\omega_{\beta}-\omega)} + \frac{\langle 0|j|\alpha\rangle\langle\alpha|k|\beta\rangle\langle\beta|i|0\rangle}{(\omega+\omega_{\beta})(\omega_{\alpha}-\omega)}\right), \tag{12}$$

$$\begin{aligned}X^{(\omega,\omega)}_{ijk}=&\frac{1}{\hbar^2}\frac{e^3N}{2!}\hat{P}_{ijk}\sum_{k}\\ &\times\sum_{\alpha,\beta,\gamma}\left(\frac{\langle 0|i|\alpha\rangle\langle\alpha|j|\beta\rangle\langle\alpha|j|\gamma\rangle\langle\gamma|l|0\rangle}{(\omega_{\gamma 0}-2\omega)(\omega_{\beta 0}-2\omega)(\omega_{\alpha 00}-\omega)}\right.\\ &+\frac{\langle 0|j|\alpha\rangle\langle\alpha|i|\beta\rangle\langle\alpha|j|\gamma\rangle\langle\gamma|l|0\rangle}{(\omega^{*}_{\gamma 0}+\omega)(\omega_{\beta 0}-2\omega)(\omega_{\alpha 00}-\omega)}\\ &+\frac{\langle 0|j|\alpha\rangle\langle\alpha|k|\beta\rangle\langle\alpha|i|\gamma\rangle\langle\gamma|l|0\rangle}{(\omega^{*}_{\gamma 0}+\omega)(\omega_{\beta 0}+2\omega)(\omega_{\alpha 00}-\omega)}\\ &\left.+\frac{\langle 0|j|\alpha\rangle\langle\alpha|k|\beta\rangle\langle\alpha|j|l\,\gamma\rangle\langle\gamma|l|0\rangle}{(\omega^{*}_{\gamma 0}+\omega)(\omega_{\beta 0}+2\omega)(\omega_{\alpha 0}+3\omega)}\right)\end{aligned} \tag{13}$$

where the $\langle\alpha|i|\beta\rangle$ are the dipole matrix momenta between the α and β electronic quasiband states, P is permutation operator, N is the concentration of the effective electron-vibration states, the summation over the **k** means summation over the whole effective molecular sphere. The TPA coefficients are evaluated as the imaginary part of the fourth rank tensors.

The use of the calculated MO electronic states and wave functions renormalized by the harmonic and anharmonic interactions allows us to estimate the time dependencies of the matrix dipole moments. In Fig. 8 are presented dependencies of calculated photoinduced SHG versus temperature and pumping power. One can clearly see good agreement with the experimental data (see Fig. 3). The observed low-temperature increase of the corresponding nonlinear susceptibilities reflects essential redistribution of the occupation between the ground and intermediate state. Polarized photoinducing power creates a large number of IR polarized

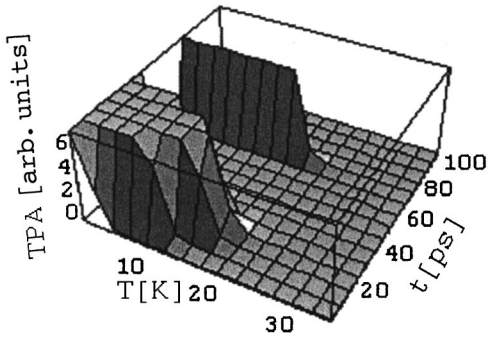

FIG. 9. Theoretically calculated dependences of the TPA for $\lambda=0.53\,\mu$m in arbitrary units versus pump-probe time delay and temperatures.

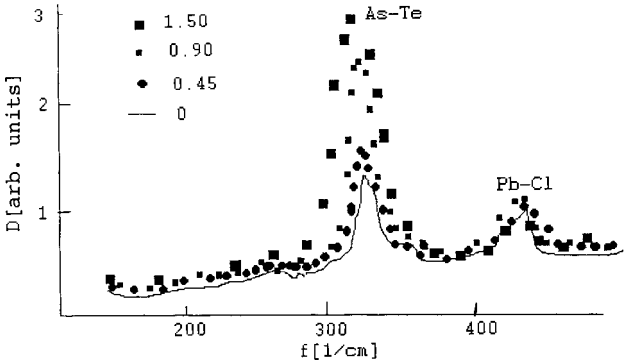

FIG. 11. FTIR measurement of the optical density D versus external photoinduced IR light of different intensity (in GW/cm^2).

phonons that, due to relatively high value of electron-vibration in the As-Te cluster, stimulate an appearance of noncentrosymmetry demonstrated in Fig. 7. The latter plays the key role in the optical SHG described by the third-order polar tensors.

The acentricity is caused mainly by the electron-quasiphonon anharmonicity described by expressions (4)–(10) and increase of temperature due to essential reorientation of the particular clusters suppress the observed noncentrosymmetry. As-Te-Ca-Cl bridges contribute also to the observed effect, but their influence is relatively weak (less than 1.6%) and it will be a subject of a separate work. The observed behavior indicates also the occurrence of a low-temperature structural rearrangement (probably ordering) of the structural fragments which can be detected by the CO-laser photoinduced SHG.

The performed calculations of temperature dependences of the TPA versus the delaying time (Fig. 8) and wavelength (Fig. 9) show also a good correlation with experimental data. Several discrepancies appear in the absolute values of the corresponding susceptibilities. From the performed calculations we have found the dominant role of the vibrations modes (within the 8–22 μm spectral range) effectively contributing (higher than 68%) to the mentioned photoinducing and temporary dependencies (see Fig. 10). An appearance of the additional delaying maxima for the TPA contrary to the SHG is the result of the fourth-step photon processes described by Eq. (13). In the case of the SHG we deal with the three-step process. As a consequence such additional step in the first case favors an appearance of additional maximum due to the retardation between the intermediate levels in Eq. (13).

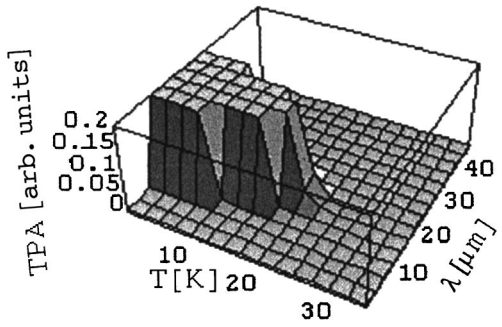

FIG. 10. Calculated spectral dependences of the TPA versus temperature.

In order to obtain information concerning the origin of the observed photoinduced changes (contribution of the particular structural fragments, partial sensitivity to the structural fragments to the IR illumination) we carry out Fourier transformation spectroscopy measurements at temperatures at about 20 K. In Fig. 11 are presented spectral dependencies of additional optical density D measured by Fourier transform infrared (FTIR) for the As_2Te_3-$CaCl_2$-$PbCl_2$ glasses. One can clearly see an essentially different change of additional absorption for the modes corresponding to the As-Te at 321 cm^{-1} and other structural fragments (for example, Pb-Cl at 430 cm^{-1}). This result confirms our calculations that the electron-vibration modes of the As-Te clusters play a key role in the observed IR photoinduced phenomena.

V. CONCLUSIONS

We have revealed an essential influence of IR laser light on the nonlinear optical susceptibilities in the As_2Te_3-$CaCl_2$-$PbCl_2$ glasses. We have shown that with an increasing photoinducing CO-laser ($\lambda=5.5\,\mu$m) exposure, the CO_2 ($\lambda=10.6\,\mu$m) SHG maximum increases and achieves its maximum at CO photon fluence 0.85–1.10 GW/cm^2 per pulse for pump-probe delaying time of about 22 ps. A good correlation between the TPA and SHG temperature dependencies was shown. The key role of the vibrations and electron-vibration anharmonicity within the 8–22 μm was revealed.

The absolute SHG values were more than one order less comparing with ZnS crystals in case of its χ_{222} ($\lambda=10.6\,\mu$m) tensor components. The relaxation time of the photoinduced SHG signal did not exceed 0.95 ps. Our molecular-dynamics geometry optimization and quantum chemical calculations unambiguously show that the photoinduced noncentrosymmetry is caused solely by the electron-quasiphonon anharmonic interaction within the As-Te terahedra. There exist at least two maxima (at 19–39 ps and 67–84 ps) in the high-resolved temporary dependences of TPA originating from the anharmonic electron-vibration renormalization of the MO electronic states in the mentioned glasses. The dominant role of the As-Te cluster contributing to nonlinear optical susceptibilities was revealed both theoretically as well by the

Fourier spectroscopy and ellipsometry measurements. Experimental data indicate an essential difference of the electron-vibration interaction in the case of the third- and fourth-rank optical susceptibilities. This difference reflects the essential asymmetry of the quasiphonon and electronic molecular-orbital states interaction for the tensors of different ranks and different temperature occupation of the particular electron-vibration states.

[1] M. Suanh and F. Shufji, Acta Phys. Sin. **24**, 235 (1997).
[2] S. Mostepanenko, Ph.D. thesis, Moscow Technical University, 1998, p. 235.
[3] J. Wasylak, J. Kucharski, I. V. Kityk, and B. Sahraoui, J. Appl. Phys. **85**, 425 (1999).
[4] X. Zhao, L. Xu, H. Yin, and S. Sakka, J. Non-Cryst. Solids **167**, 70 (1994).
[5] S. A. Solin and G. N. Papatheodorou, Phys. Rev. B **15**, 2084 (1977).
[6] J. P. de Neufville, S. C. Moss, and S. R. Ovshinsky, J. Non-Cryst. Solids **13**, 191 (1974).
[7] K. Tanaka, Solid State Commun. **15**, 1521 (1974).
[8] J. S. Berkes, S. W. Ing, and W. J. Hillegas, J. Appl. Phys. **42**, 4908 (1971).
[9] K. Tanaka, Appl. Phys. Lett. **26**, 243 (1975).
[10] R. A. Street, Phys. Rev. B **17**, 3984 (1978).
[11] V. Halpern, Philos. Mag. **34**, 331 (1976).
[12] V. I. Vlasov and D. G. Semak, Ukr. Phys. J. **22**, 2053 (1977).
[13] V. K. Malinovsky and V. G. Zhdanov, J. Non-Cryst. Solids **51**, 31 (1982).
[14] S. A. Dembovsky and E. A. Chechetkina, J. Non-Cryst. Solids **64**, 95 (1984).
[15] E. Golis, I. V. Kityk, J. Wasylak, and J. Kasperczyk, Mater. Res. Bull. **31**, 1057 (1996).
[16] J. Zyss and D. S. Chemla, *Quantum Electronics (Principles and Applications)* (Academic Press, New York, 1987), Vols. 1 and 2.
[17] M. Frumar, A. F. Firth, and A. E. Owen, J. Non-Cryst. Solids **59-67**, 987 (1983).
[18] S. R. Elliott, J. Non-Cryst. Solids **81**, 71 (1986).
[19] E. V. Pirogov and K. K. Shvarts, J. Non-Cryst. Solids **97-98**, 1211 (1987).
[20] B. Kalwin and R. Steart, Glass Technol. **3**, 104 (1997).
[21] Ya. O. Dovgii and I. V. Kityk, Fiz. Tverd. Tela (Leningrad) **33**, 416 (1991) [Sov. Phys. Solid State **33**, 238 (1991)].
[22] A. D. Becke, J. Chem. Phys. **98**, 1372 (1994); **98**, 5648 (1994).
[23] M. J. Frisch, G. W. Trucks, H. W. Schlegel, P. M. W. Gill, B. G. Johnson, M. W. Wong, J. B. Foresman, M. Head-Gordon, E. S. Replogle, R. Gomperts, J. L. Andres, K. Raghvachari, J. S. Binkley, C. Gonzales, R. L. Martin, D. J. Fox, D. Defrees, J. Baker, J. J. P. Stewart, and J. A. Pople, GAUSSIAN94, Rev. C3 (Gaussian Inc., Pittsburgh, 1994).
[24] D. E. Woon and T. H. Dunning, J. Chem. Phys. **98**, 1358 (1993).
[25] GAMES, *General Atomic and Molecular Electronic Structure System*, 1990, Vol. 10, p. 52.
[26] H. L. Skriver, *The Linear Muffin Tin Orbitals Method* (Springer, Berlin, 1984).
[27] I. V. Kityk, J. Kasperczyk, and B. V. Andrievskii, Phys. Lett. A **216**, 161 (1996).
[28] A. S. Davydov, *Introduction to the Solid State Physics* (Nauka, Moscow, 1987) (in Russian).